Proceedings of the 9th RSI
International Conference on Robotics and Mechatronics (ICRoM 2021)
Nov. 17-19, 2021, Tehran, Iran

2021 9th RSI International Conference on Robotics and Mechatronics (ICRoM) | 978-1-6654-2094-5/21/$31.00 ©2021 IEEE | DOI: 10.1109/ICRoM54204.2021.9663516

Kinematic and Dynamic Analysis of ARASH ASiST: Toward Micro Positioning

A. Hassani*, M.R. Dindarloo*, R. Khorambakht*, A. Bataleblu*, H. Sadeghi*, R. Heidari*, A. Iranfar*,
P. Hasani*, N.S. Hojati*, A. Khorasani*, N. KhajeAhmadi*, M. Motaharifar†,
H. Riazi-Esfahani‡, A. Lashay‡, S. F. Mohammadi‡, H. D. Taghirad*
* Advanced Robotics and Automated Systems (ARAS), K.N. Toosi University of Technology, Tehran, Iran.
† Department of Electrical Engineering, University of Isfahan, Isfahan, Iran.
‡ Translational Ophthalmology Research Center, Farabi Eye Hospital,
Tehran University of Medical Sciences, Tehran, Iran.
Email: *taghirad@kntu.ac.ir, †m.motaharifar@eng.ui.ac.ir,
‡h-riazi@razi.tums.ac.ir, lashay@tums.ac.ir, sfmohammadi@tums.ac.ir

***Abstract*—This article elaborate on the kinematic and dynamic analysis of ARASH:ASiST, "ARAS Haptic System for Eye Surgery Training", which is developed for vitrectomy eye surgery training. The mechanism selection of this system is reviewed first, in order to assist such a precise intraocular eye surgery training. Then the kinematics and dynamics analysis of the proposed haptic system is investigated. To verify the reported result, a prototype of ARASH:ASiST is modeled in MSC-ADAMS®, and the results of the dynamic formulation are validated. Finally, a common model-based controller is implemented on the real prototype, and it is verified that with such controller a suitable accuracy of $200\ \mu m$ is attainable for the surgical instrument.**

***Index Terms*—ARASH:ASiST, Robot-Assisted Surgery, Vitrectomy, Haptic System, Dynamics Analysis, Precisions.**

I. Introduction

One of the leading causes of blindness is retinal diseases, and vitro-retinal surgeries are commonly used for treatment. Among the common pathologies related to the vitreoretinal operation, retinal detachment, vitreous hemorrhage, macular pucker, macular hole, and diabetic retinopathy are noteworthy [1]. Vitrectomy surgery, which is considered in this paper, is defined as removing and replacing vitreous humor [2]. An illustration of vitrectomy eye surgery can be seen in Fig. 1.

Vitrectomy surgery includes micro-surgical procedures and is considered to be one of the most challenging operations in medical science [3]. In this surgery, the surgeons must carefully control the position and force of the small surgical instrument (called vitrector) in a limited workspace with a delicate positioning accuracy of $10\mu m$ (which is less than the average amplitude of hand tremors) [4]. Furthermore, it is tiresome to maintain the vitrector for a long period of time in this limited workspace due to the physical, visual, and mental fatigue of surgeons [1]. Estimating the distance between the tip of the vitrector and the tissue with microscopic vision is also very challenging, due to lack of sense of touch, and this challenge is more pronounced for novice surgeons [4].

To address these problems, the use of robotic technology is recommended. Robots can provide high motion accuracy and dexterity needed to perform micro-surgeries, and by providing a comfortable and ergonomic environment for surgeons, surgical efficiency will certainly increase [5]. In the last decade, various microsurgical robots for vitreoretinal surgeries have been developed and among these robots, steady hand manipulator (SHM) [6], intraocular robotic interventional surgical system (IRISS) [7], PRECEYES micromanipulator [8], ARAS DIAMOND spherical robot [9], and modified Da Vinci surgeon robot [10] may be listed. It is worth mentioning that the first experimental robotic vitreoretinal eye surgery was performed clinically using PRECEYES [11].

With the increasing development of microsurgical robots for vitreoretinal eye surgeries, the training process for novice surgeons can also be evaluated [12]. In traditional eye surgery training, the trainer holds the novice's hands to correct his/her movements. Such a process is complicated for the trainer, and the training time is extended. Therefore, the robotic surgical training systems may be used to provide the required accuracy and feedback to the novice surgeons with trainer direct involvement [13]. In such a system, the surgery is performed by the trainer, and the novice learns the skills by obtaining haptic feedback. By gaining sufficient skills, the trainee performs the surgery directly with the trainer's

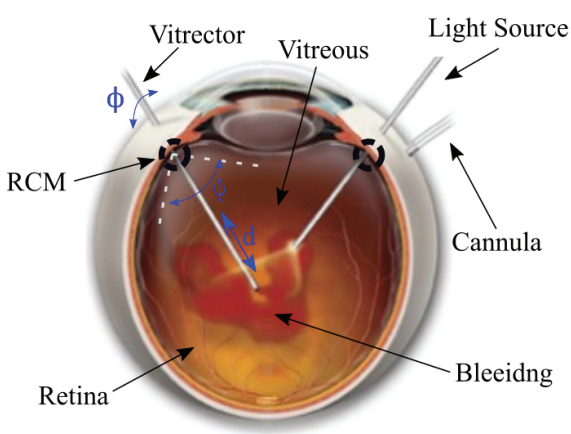

Fig. 1. Overview of Vitrectomy Eye Surgery

Fig. 2. ARASH:ASiST in the operating room

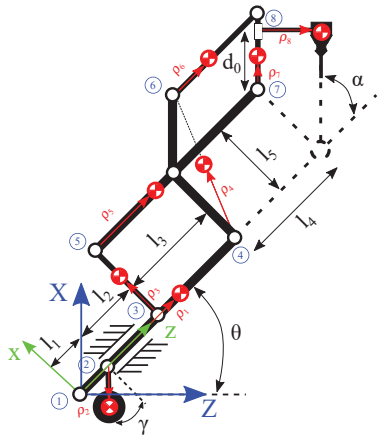

Fig. 3. Overview of ARASH:ASiST mechanism

supervision. To avoid undesired complications, the trainer can interfere within the procedure in the case of sudden mistakes that may cause irreversible complications [14].

Considering the presented idea, this paper examines dynamic analysis and micro positioning of ARASH:ASiST, "ARAS Haptic System for EYE Surgery Training". This haptic system is an intraocular eye surgery training system developed to train novice surgeons in vitrectomy surgeries. A view of the ARASH:ASiST system may be seen in Fig. 2.

In this paper, the required mechanism to perform a precise vitrectomy eye surgery training system is reviewed, and then, the kinematic and dynamic analysis of the considered mechanism is carefully examined. To validate the dynamic model, a prototype of ARASH:ASiST is built in MSC-ADAMS®, and the results of the dynamic formulation are verified. Finally, the precise motion tracking of the consoles is examined using a model-based controller.

II. Mechanism Selection

In this section, the selected mechanism of the ARASH:ASiST will be reviewed, whose overview is shown in Fig. 3. The details of the mechanism given in this figure are elaborated.

A. Remote Center of Motion (RCM)

One of the main features required in minimally-invasive surgery (MIS) is the remote center of motion (RCM). In the surgical process, the surgical instrument (known as a vitrector in vitrectomy eye surgery) enters the patient's eye through a small incision, and the surgery process takes place about this pivot point. Thus, the rotational movements of the robot about this pivot point should not affect the motion of the vitrector, while the incision shall be not enlarged. There are several ways to create a mechanical RCM, which may be listed as isocenters, circular tracking arcs, parallelograms, spherical linkages, and synchronous belt transmissions [15]. Among these methods, the parallelogram-based RCM mechanism is the most popular choice in MIS robotic surgery [16]. In ARASH:ASiST, double parallelogram mechanisms have been used to create the RCM in the robot. The most important reasons for this choice are the simplicity of mechanism structure and the possibility of placing the actuators at the base [17].

B. Degrees of Freedom (DOF)

Four degrees of freedom (DOF) are suggested [18], for full in vitro-retinal surgeries. Among those, three rotations (ϕ, ψ, β) and linear motion (d) in the axial direction are needed. However, to fully cover the required spherical workspace for vitrectomy eye surgery, only ϕ and ψ are needed, and the spin of the vitrector is not used [19]. Moreover, according to the comments of vitrectomy experts in the operational trials of the mechanism, θ inclination of the mechanism is adjusted to cover an ergonomic workspace in the vitrectomy eye surgery.

C. Weight Compensation

Weight compensation in robot–assisted surgery systems is essential since it makes it easier for the surgeon to work with the haptic system in free mode (without a controller), while the weight of the system will not disturb the common hand trajectories of the surgeons. Weight compensation will reduce the control effort in the control loop, as well, and allows optimal power consumption in the actuators. For this purpose, two symmetrical weight counterbalances (WCs) are considered to compensate for the weight of the rotational DOF of the robot. To ensure high reliability and eliminate the probability of collision weights with the patient head and surgeon's hand, WCs are located at the end of the mechanism and near the base. Due to the limited space of the end-effector, it is not possible to design a fully passive compensation mechanism for gravity compensation of the vitrector, and the use of active methods is inevitable.

III. Kinematic Analysis

A. Forward Kinematic

For forward kinematic analysis, the successive screw method [20] has been used. The locations of the screw axes with respect to the base coordinate system are listed in Table I. In this analysis, it is assumed that the tip of the vitrector is at

the RCM point, and by moving the vitrector downward (within the eye), the space required to cover the vitrectomy operation will be obtained. Moreover, $\boldsymbol{q} = [\phi, \psi, d]^T$ represents the actuated joints variables, and l_{1234} indicated $l_{1234} = l_1 + l_2 + l_3 + l_4$. Therefore, the reference position of vitrector is defined as:

$$\boldsymbol{T}_0 = \begin{bmatrix} \boldsymbol{I}_{3\times3} & [0, 0, l_{1234} + d]^T \\ \boldsymbol{0}_{1\times3} & 1 \end{bmatrix} \tag{1}$$

Therefore, the homogeneous transformation matrix of the vitrector with respect to the base coordinate frame XYZ may be derived as follow:

$${}^0\boldsymbol{T}_v = \left({}^0\boldsymbol{T}_1\ {}^1\boldsymbol{T}_2\ {}^2\boldsymbol{T}_3\right)\boldsymbol{T}_0 = \begin{bmatrix} {}^0\boldsymbol{R} & {}^0\boldsymbol{p} \\ \boldsymbol{0}_{1\times3} & 1 \end{bmatrix} \tag{2}$$

in which, the position vector ${}^0\boldsymbol{p} = [x, y, z]^T$ and rotation matrix ${}^0\boldsymbol{R}$ of the vitrector is reported in Eqs. (3), (4). It should be noted that in this equation, s_ϕ and c_ϕ denote $sin(\phi)$ and $\cos(\phi)$, respectively.

$${}^0\boldsymbol{p} = \begin{bmatrix} d(+c_\theta c_\phi s_{\psi+\alpha} + s_\theta c_{\psi+\alpha}) + l_{1234} s_\theta \\ d s_\phi s_{\psi+\alpha} \\ d(-s_\theta c_\phi s_{\psi+\alpha} + c_\theta c_{\psi+\alpha}) + l_{1234} c_\theta \end{bmatrix} \tag{3}$$

$${}^0\boldsymbol{R} = \begin{bmatrix} c_\theta c_\phi c_{\psi+\alpha} - s_\theta s_{\psi+\alpha} & -c_\theta s_\phi & c_\theta c_\phi s_{\psi+\alpha} + s_\theta c_{\psi+\alpha} \\ s_\phi c_{\psi+\alpha} & c_\phi & s_\phi s_{\psi+\alpha} \\ -s_\theta c_\phi c_{\psi+\alpha} - c_\theta s_{\psi+\alpha} & s_\theta s_\phi & -s_\theta c_\phi s_{\psi+\alpha} + c_\theta c_{\psi+\alpha} \end{bmatrix} \tag{4}$$

B. Robot Workspace

By carefully examining the work-space of the eye and according to the opinion of vitrectomy specialists, the required actuated joint motions are set as $-45° \leq \phi \leq 45°$, $-30° \leq \psi \leq 60°$ and $-27mm \leq d \leq 16mm$. This workspace is accessible for the robot shown in Fig. 4, with the specific design parameters considered for the robot, as reported in Table. II.

C. Jacobian Analysis

The Jacobian matrix is of utmost importance in the differential kinematics analysis of the robot. Jacobian maps actuator joint variables $\dot{\boldsymbol{q}}$ to the end-effector velocities, and

TABLE I
SCREW AXES PARAMETERS OF ARASH:ASIST

Joint i	Joint Variable	$\boldsymbol{s}_i$	$\boldsymbol{s}_{oi}$
1	θ	$[0, 1, 0]^T$	$[0, 0, 0]^T$
2	ϕ	$[0, 0, 1]^T$	$[0, 0, 0]^T$
3	$\psi + \alpha$	$[0, 1, 0]^T$	$[0, 0, l_{1234}]^T$

TABLE II
DESIGN PARAMETERS OF ARASH:ASIST

Parameter	l_1	l_2	l_3	l_4	α	θ	γ
Quantity	$6mm$	$176mm$	$50mm$	$115m$	50°	42°	20°

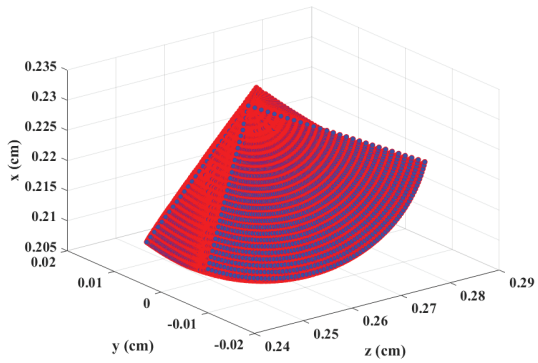

Fig. 4. Designed workspace for minimally invasive vitreoretinal surgery

furthermore, the actuator forces to forces applied to the end-effector. The Jacobian matrix $\boldsymbol{J} = [\boldsymbol{J}_v, \boldsymbol{J}_\omega]^T$ consists of two linear and angular parts. To extract the linear part of Jacobian matrix, the partial derivative from ${}^0\boldsymbol{p}$ with respect to $\boldsymbol{q}$ shall be derived. Moreover, the angular velocity of the vitrector may be derived as:

$${}^0\boldsymbol{\omega} = \boldsymbol{R}_\theta [0, 0, \dot{\phi}]^T + \boldsymbol{R}_\theta \boldsymbol{R}_\phi [0, \dot{\psi}, 0]^T \tag{4}$$

in which, $\boldsymbol{R}_\theta$ and $\boldsymbol{R}_\phi$ represent $\boldsymbol{R}_\theta = \boldsymbol{R}_y(\theta)$ and $\boldsymbol{R}_\phi = \boldsymbol{R}_z(\phi)$, respectively. Therefore by categorizing ${}^0\boldsymbol{\omega}$ as $\dot{\boldsymbol{q}} = [\dot{\phi}, \dot{\psi}, \dot{d}]^T$, $\boldsymbol{J}_\omega$ can be easily extracted. The final result of the Jacobian matrix is reported in Eq. (5).

D. Singularity Analysis

In order to investigate the singularity configurations of the robot, the determinant of $\boldsymbol{J}_v$ may be derived as:

$$\det(\boldsymbol{J}_v) = -d^2 \times \sin(\psi + \alpha) \tag{6}$$

Therefore, the singularities are divided into two groups:

1) Parallelogram mechanism singularity: this may occur when $\psi + \alpha = k\pi$. According to the designed $\boldsymbol{q}$ range, $\psi + \alpha \neq k\pi$, but $\psi = -\alpha$ occurs only when the parallelogram mechanism reaches the end of its range therefore we do not see any singularity of this type during the operation.
2) Remote center of motion (RCM) singularity: In this singularity ($d = 0$), the change in the ϕ and ψ does not affect the motion of the vitrector, which is an important and desired future in MIS.

IV. DYNAMIC ANALYSIS

A. Kinematic Analysis of Links

To simplify the dynamics formulations of the robot, the fixed xyz coordinate system is used and named as 0 in the following formulations. Therefore by removing the θ variable from the Jacobian equations of robot links and adding its effect to the gravity vector, the dynamics formulations of the robot will be extracted more efficiently. A complete overview of robot links can be seen in Fig. 2.

$$\boldsymbol{J} = \begin{bmatrix} -dc_\theta s_\phi s_{\psi+\alpha} & -d\left(-c_\theta c_\phi c_{\psi+\alpha} + s_\theta s_{\psi+\alpha}\right) & c_\theta c_\phi s_{\psi+\alpha} + s_\theta c_{\psi+\alpha} \\ dc_\phi s_{\psi+\alpha} & ds_\phi c_{\psi+\alpha} & s_\phi s_{\psi+\alpha} \\ ds_\theta s_\phi s_{\psi+\alpha} & -d\left(+s_\theta c_\phi c_{\psi+\alpha} + c_\theta s_{\psi+\alpha}\right) & -s_\theta c_\phi s_{\psi+\alpha} + c_\theta c_{\psi+\alpha} \\ s_\theta & -c_\theta s_\phi & 0 \\ 0 & c_\phi & 0 \\ c_\theta & s_\theta s_\phi & 0 \end{bmatrix} \tag{5}$$

1) Joint Analysis: According to Fig. 2, the position of the coordinate frame system J_i, which is located in the initial joint of each link and denoted as $\boldsymbol{p}_{J_i}$, may be given by:

$$^0\boldsymbol{p}_{\mathrm{J}_1} = \begin{bmatrix} 0 & 0 & 0 \end{bmatrix}^T \ , \ ^0\boldsymbol{p}_{\mathrm{J}_2} = (l_1)\hat{\boldsymbol{z}} \ , \ ^0\boldsymbol{p}_{\mathrm{J}_3} = (l_{12})\hat{\boldsymbol{z}} \tag{7a}$$

$$^0\boldsymbol{p}_{\mathrm{J}_4} = (l_{123})\hat{\boldsymbol{z}} \ , \ ^0\boldsymbol{p}_{\mathrm{J}_5} = \boldsymbol{R}_\phi \ \boldsymbol{R}_\psi \left(l_5\hat{\boldsymbol{x}} + l_{12}\hat{\boldsymbol{z}}\right) \tag{7b}$$

$$^0\boldsymbol{p}_{\mathrm{J}_6} = \boldsymbol{R}_\phi \ \boldsymbol{R}_\psi \left(l_{x_{46}}\hat{\boldsymbol{x}} + (l_{z_{46}} + l_{123})\,\hat{\boldsymbol{z}}\right) \tag{7c}$$

$$^0\boldsymbol{p}_{\mathrm{J}_7} = \boldsymbol{R}_\phi \ \boldsymbol{R}_\psi \left(l_5\hat{\boldsymbol{x}} + l_{1234}\hat{\boldsymbol{z}}\right) \tag{7d}$$

$$^0\boldsymbol{p}_{\mathrm{J}_8} = \ ^0\boldsymbol{p}_{\mathrm{J}_7} + \boldsymbol{R}_\phi \ \boldsymbol{R}_\psi \ \boldsymbol{R}_\alpha \ \left((d + d_0)\hat{\boldsymbol{z}}\right) \tag{7e}$$

in which, $\hat{\boldsymbol{x}}$ and $\hat{\boldsymbol{z}}$ denote the unit vector of x and z axis in the xyz base coordinate system, and l_{12} and l_{123} denote $l_{12} = l_1 + l_2$ and $l_{123} = l_1 + l_2 + l_3$, respectively. Moreover $\boldsymbol{R}_\psi$ and $\boldsymbol{R}_\alpha$ represent $\boldsymbol{R}_\psi = \boldsymbol{R}_y(\psi)$ and $\boldsymbol{R}_\alpha = \boldsymbol{R}_y(\alpha)$.

According to Fig. 2 and due to the existence of a parallelogram property in the robot, the rotation matrix of each link (which is equal to the orientation of the coordinate frame system J_i) with respect to the base coordinate system may be derived as follows:

$$^0\boldsymbol{R}_i = \boldsymbol{R}_\phi \ , \text{ for i=1,5,6} \tag{8a}$$

$$^0\boldsymbol{R}_i = \boldsymbol{R}_\phi \ \boldsymbol{R}_\psi \ , \text{ for i=3,4,7} \tag{8b}$$

$$^0\boldsymbol{R}_i = \boldsymbol{R}_\phi \ \boldsymbol{R}_\psi \ \boldsymbol{R}_\gamma \ , \text{ for i=2} \tag{8c}$$

2) Center of Gravity Analysis: The position of the center of gravity (CG) of each link may be derived as follow:

$$^0\boldsymbol{p}_{G_i} = \ ^0\boldsymbol{R}_i \ ^i\boldsymbol{\rho}_i + \ ^0\boldsymbol{p}_{J_i} \ , \text{ for i=1,..,8} \tag{9}$$

in which, $^i\boldsymbol{\rho}_\mathrm{i}$ denotes the CG vector of each link, respect to its local coordinate system.

B. Jacobian Analysis of Links

Similar to the process mentioned in section III-C, the linear Jacobian of CG of robot link may be derived by taking the partial derivative from the $^0\boldsymbol{p}_{G_i}$ with respect to $\boldsymbol{q}$. Moreover, the angular part of the Jacobian matrix of each link may be derived as:

$$\boldsymbol{J}_{\omega_i} = \begin{bmatrix} 0 & 0 & 0 \\ 0 & 0 & 0 \\ 1 & 0 & 0 \end{bmatrix} \ , \text{ for i=1,5,6} \tag{10a}$$

$$\boldsymbol{J}_{\omega_i} = \begin{bmatrix} 0 & -s_\phi & 0 \\ 0 & c_\phi & 0 \\ 1 & 0 & 0 \end{bmatrix} \ , \text{ for i=2,3,4,7,8} \tag{10b}$$

C. Explicit Dynamics Formulation

By neglecting the effect of frictions, dynamics of actuators, and other possible disturbances, it is common to express the closed-form dynamics of manipulators in the explicit form as [20]:

$$\boldsymbol{M}(\boldsymbol{q})\ddot{\boldsymbol{q}} + \boldsymbol{C}(\boldsymbol{q}, \dot{\boldsymbol{q}})\dot{\boldsymbol{q}} + \boldsymbol{g}(\boldsymbol{q}) = \boldsymbol{\tau} \tag{11}$$

where $\boldsymbol{M}(\boldsymbol{q})$ is the symmetric positive definite mass matrix, $\boldsymbol{C}(\boldsymbol{q}, \dot{\boldsymbol{q}})$ is the centrifugal and Coriolis matrix, $\boldsymbol{g}(\boldsymbol{q})$ is the gravitational vector and $\boldsymbol{\tau}$ is the generalized actuators forces $\boldsymbol{\tau} = [\tau_\phi, \tau_\psi, f_d]^T$. For serial robots, it can be shown that the various parts of explicit dynamics are extracted as follows [20]:

$$\boldsymbol{M}(\boldsymbol{q}) = \sum_{i=1}^{8} \left(\boldsymbol{J}_{v_{G_i}}{}^T \ m_i \ \boldsymbol{J}_{v_{G_i}} + \boldsymbol{J}_{\omega_i}{}^T \ ^0\boldsymbol{I}_{G_i} \ \boldsymbol{J}_{\omega_i} \right) \tag{12a}$$

$$C_{ij}(\boldsymbol{q}, \dot{\boldsymbol{q}}) = \sum_{k=1}^{8} \frac{1}{2} \left(\frac{\partial M_{ij}}{\partial q_k} + \frac{\partial M_{ik}}{\partial q_j} - \frac{\partial M_{jk}}{\partial \boldsymbol{q}_i} \right) \dot{q}_k \tag{12b}$$

$$\boldsymbol{g}(\boldsymbol{q}) = -\sum_{i=1}^{8} m_i \ \boldsymbol{g}_0{}^T \ \boldsymbol{J}_{v_{G_i}} \tag{12c}$$

in which, $\boldsymbol{g}_0 = \boldsymbol{R}_\theta{}^T \left[-9.81, 0, 0\right]^T$. To derive equations (12a) to (12c) in symbolic form, symbolic software Maple is used. Complete results of explicit dynamics are publicly available in [21].

D. Verification

To validate all the kinematic and dynamic equations of the robot, MSC-ADAMS® software is used. An overview of the robot model in MSC-ADAMS® software can be seen in Fig. 5.

To verify the inverse dynamics of the robot, it is assumed that $\boldsymbol{q}$ is defined and the torque $\boldsymbol{\tau}$ required to track $\boldsymbol{q}$ should be calculated. Validation trajectories are defined as $\phi = 45^\circ \sin(4\pi t)$, $\psi = 45^\circ \sin(3\pi t) + 15^\circ$, and $d = 15mm \ \sin(4\pi t)$. Then, these trajectories are given to the robot model in the MSC ADAMS®, and the explicit robot dynamic model (11). The result is shown in Fig. 6.

As it is seen in Fig. 6, the explicit dynamic model and ADAMS model is quite identical, at the order of 10^{-4}. Moreover, the same results are obtained when applying other trajectories, such as the third-order polynomial and multi-sine trajectories.

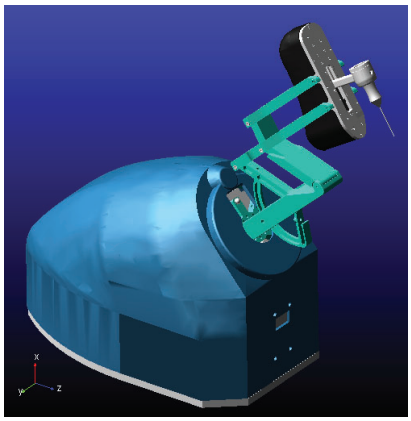

Fig. 5. ARASH:ASiST model in MSC ADAMS®

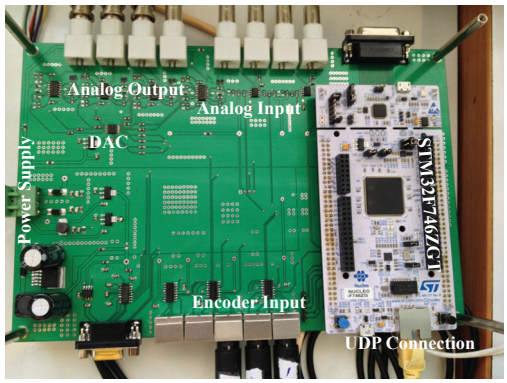

Fig. 7. View of the designed data acquisition for ARASH:ASiST

E. Effect of Gravity Compensation

To evaluate the effect of adding WCs to the amount of actuator torque $\boldsymbol{\tau}$, the robot has been moved through its entire workspace, and the values of the $\boldsymbol{\tau}$ are calculated for both cases when there is no mass counterbalance, and when there is mass counterbalance in the system. In the absence of mass counterbalances $\|\tau_{G1}\| = 2.9755\ N.m$, $\|\tau_{G2}\| = 7.7658\ N.m$, while this is significantly reduced to $\|\tau_{G1}\| = 0.9438\ N.m$, $\|\tau_{G2}\| = 1.9529\ N.m$, when the counterbalance is in effect. This will ensure using the maximum power of the actuators in the motion/force interaction applied to the surgeon's hand.

V. Motion Tracking

A. Real-time Embedded System

Using the robot dynamic model, the values of $\boldsymbol{\tau}$ in the robot workspace are calculated. By designing transmission ratio $n_\phi = n_\psi = 5$ for rotational DOFs, and $n_d = 20$ for linear DOF, and considering reliability coefficient 1.5, the required torques for the motors are calculated. Thus, Maxon EC-max30 and Maxon EC-max22 are selected for rotational DOFs and linear DOF, respectively. These motors are equipped with HELD 5540, 500 CPT, and MR, 512 CPT incremental encoders, respectively, to measure the actuated joint angles. Moreover, to drive the motors, Maxon EPOS2 36/2 controller has been used, and the drivers are set in current control mode.

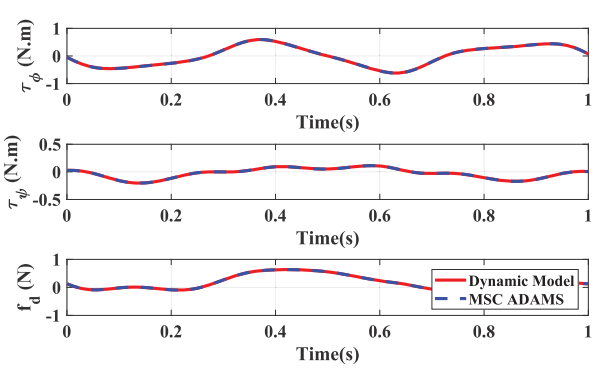

Fig. 6. Explicit dynamics verification

In order to facilitate the development cycle and analysis procedures, we adopt the Matlab Simulink Real-Time framework. The algorithms are defined as Simulink models on a host computer and then translate it into codes that run on an X86 target PC through an Ethernet connection. Simulink Real-Time supports many standard Data Acquisition (DAQ) cards and general interfaces such as Ethernet and RS-232. In this paper, we have embedded the data acquisition hardware into the structure of our robot instead of relying on commercial PCI cards. Other than being a less expensive solution, this choice provides a unified hardware framework that is applicable during both the development and final product phases. This system has been implemented by adding an Ethernet interface to the embedded controller through which a UDP communications link with the target computer is established. Our embedded system is based on an ARM CORTEX-M7 microcontroller with enough computational capacity to act as the data bridge and execute advanced controllers and observers with demanding computational loads.

As illustrated in Fig. 7, the embedded controller is located between the target computer and the robot. The sampling rate of the communication link is set to $1\ kHz$, which is sufficient considering the fastest dominant transients of the robot and the reference trajectories. The received control commands from the target computer are fed to an SPI DAC chip that generates the analog torque commands to the motor driver (current control mode). In return, the microcontroller decodes the motor encoder signals and sends them back to the target computer.

B. Controller Design

In this section, the results of motion tracking by one of the ARASH:ASiST consoles are reported. In this paper, the inverse dynamic controller (IDC) is chosen as the first experimental design for further developments. It is worth noting that IDC is a general and effective controller that is the basis for many advanced model-based controllers [22]. The control effort of this controller is given as follows:

$$\boldsymbol{\tau} = \hat{\boldsymbol{M}}(\boldsymbol{q})\left(\ddot{\boldsymbol{q}}_d + \boldsymbol{K}_v\dot{\boldsymbol{e}} + \boldsymbol{K}_p\boldsymbol{e}\right) + \hat{\boldsymbol{C}}(\boldsymbol{q},\dot{\boldsymbol{q}})\dot{\boldsymbol{q}} + \hat{\boldsymbol{g}}(\boldsymbol{q}) \quad (13)$$

in which, $\boldsymbol{e} = \boldsymbol{q}_d - \boldsymbol{q}$ defines the tracking error, the desired trajectory in joint space is denoted by $\boldsymbol{q}_d$, and $\boldsymbol{q}$ denotes the measured joint space variable. Furthermore, $\hat{\boldsymbol{M}}(\boldsymbol{q})$, $\hat{\boldsymbol{C}}(\boldsymbol{q}, \dot{\boldsymbol{q}})$, and $\hat{\boldsymbol{g}}(\boldsymbol{q})$ represent the nominal values of the manipulator mass matrix, Coriolis and centrifugal matrix, and gravity vector, respectively. The PD controller gains are denoted by $\boldsymbol{K}_p$ and $\boldsymbol{K}_v$. In general, Eq. (13) is designed to control the vitrector in the joint space. It should be noted that due to the presence of RCM point in the kinematic structure of the robot, and the decoupled structure of the robot mechanism, spherical coordinate system $\boldsymbol{q} = \boldsymbol{x} = [\phi, \psi, d]^T$ are preferably used to describe the vitrector motion in the task-space [9], [23].

Thus, $\phi_d = 40° \sin(0.5t)$, $\psi_d = 40° \sin(0.5t) + 15°$ and $d_d = 1.3cm \ \sin(0.5t)$ are considered at the desired trajectory, and, the controller gains ate set to $\boldsymbol{K}_p = diag(500, 750, 325)$, and $\boldsymbol{K}_v = diag(3, 2, 0.125)$. The tracking results are reported in Figures 8 to 10.

As shown in Fig. 8, the vitrector has favorably tracked desired trajectory in the workspace. Examination of Fig. 9 also shows that the maximum vitrector error in tracking a sinusoidal trajectory is 223 μm which is very suitable for such simple controller structure. Furthermore, by examining Fig. 10, it is clear that the control effort is also very smooth and easily implementable.

It should be noted that the nominal parameters of the robot (which are extracted from the CAD model of the robot and datasheets of motors) are used as the nominal values for the IDC matrices. The effect of the structured uncertainty (such as unmodulated dynamic terms such as the elastic effect of transmission cables, friction of joints, and motor dynamics) and parametric uncertainties in the robot structure on the tracking performance may be significantly reduced through an experimental calibration process of the robot, which is under current study.

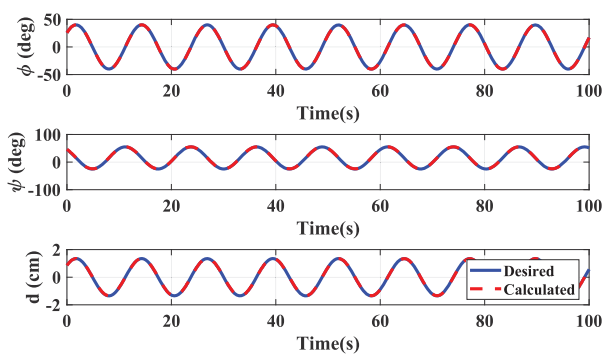

Fig. 8. Motion tracking of ARASH:ASiST, with IDC controller

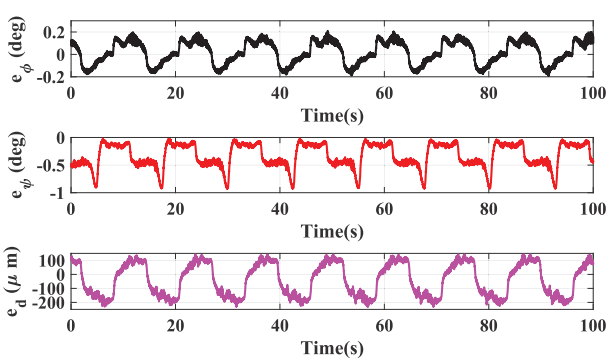

Fig. 9. Motion tracking error of ARASH:ASiST, with IDC controller

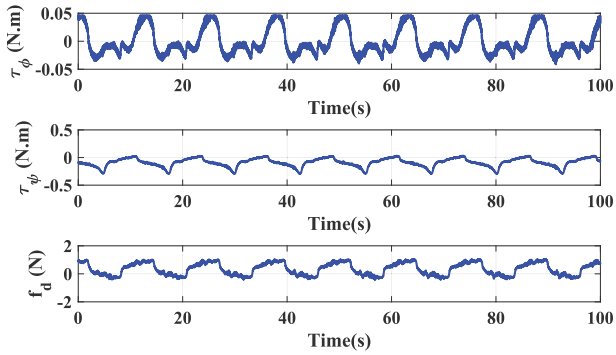

Fig. 10. Control effort of ARASH:ASiST, with IDC controller

VI. Conclusions

In this paper, the dynamic analysis and accurate motion control of ARASH:ASiST are reported briefly. ARASH:ASiST stands for "ARAS haptic system for eye surgery training, which is an eye surgery training system developed to train novice surgeons in vitrectomy surgeries. This paper investigates the required mechanical mechanism to perform such delicate operations. Furthermore, it briefly reports the major kinematic and explicit dynamics of the mechanism. The results of the dynamic formulation are numerically validated using MSC-ADAMS®. In addition, inverse dynamic controller (IDC), which is the basis for many advanced model-based controllers, is implemented on the robot to evaluate the precision of motion tracking of one of the consoles. The results show a suitable tracking error of about 200 μm for surgical instrument. The ongoing research on this system includes,

1) Kinematic [24], [25] and dynamic calibration of the robot [26], [27], to reduce the effects of structured and parametric uncertainties on the tracking performance.
2) Skill assessment of novice surgeons, using probabilistic [28] and machine learning approaches.
3) A General and comprehensive data set collection and tagging by the vitrectomy expert surgeons, using ARASH:ASiST, called ARAS-Farabi Cataract Dataset (AFCID).

Acknowledgment

This work was supported in part by the National Institute for Medical Research Development (NIMAD) under Grant No. 4000031, and Iran National Science Foundation (INSF) Synergy Grant No. 99021926. The collaboration of our national and international collaborators are acknowledged and highly appreciated.

REFERENCES

1 I. Fleming, M. Balicki, J. Koo, I. Iordachita, B. Mitchell, J. Handa, G. Hager, and R. Taylor, "Cooperative robot assistant for retinal microsurgery," in *International conference on medical image computing and computer-assisted intervention*. Springer, 2008, pp. 543–550.

2 H. Meenink, R. Hendrix, G. Naus, M. Beelen, H. Nijmeijer, M. Steinbuch, E. van Oosterhout, and M. de Smet, "Robot-assisted vitreoretinal surgery," in *Medical Robotics*. Elsevier, 2012, pp. 185–209.

3 X. He, V. Van Geirt, P. Gehlbach, R. Taylor, and I. Iordachita, "Iris: integrated robotic intraocular snake," in *2015 IEEE International Conference on Robotics and Automation (ICRA)*. IEEE, 2015, pp. 1764–1769.

4 Y. Ida, N. Sugita, T. Ueta, Y. Tamaki, K. Tanimoto, and M. Mitsuishi, "Microsurgical robotic system for vitreoretinal surgery," *International journal of computer assisted radiology and surgery*, vol. 7, no. 1, pp. 27–34, 2012.

5 S. Najarian, M. Fallahnezhad, and E. Afshari, "Advances in medical robotic systems with specific applications in surgery—a review," *Journal of medical engineering & technology*, vol. 35, no. 1, pp. 19–33, 2011.

6 A. Üneri, M. A. Balicki, J. Handa, P. Gehlbach, R. H. Taylor, and I. Iordachita, "New steady-hand eye robot with micro-force sensing for vitreoretinal surgery," in *2010 3rd IEEE RAS & EMBS International Conference on Biomedical Robotics and Biomechatronics*. IEEE, 2010, pp. 814–819.

7 E. Rahimy, J. Wilson, T. Tsao, S. Schwartz, and J. Hubschman, "Robot-assisted intraocular surgery: development of the iriss and feasibility studies in an animal model," *Eye*, vol. 27, no. 8, pp. 972–978, 2013.

8 M. D. de Smet, T. C. Meenink, T. Janssens, V. Vanheukelom, G. J. Naus, M. J. Beelen, C. Meers, B. Jonckx, and J.-M. Stassen, "Robotic assisted cannulation of occluded retinal veins," *PloS one*, vol. 11, no. 9, p. e0162037, 2016.

9 A. Molaei, E. Abedloo, H. D. Taghirad, and Z. Marvi, "Kinematic and workspace analysis of diamond: An innovative eye surgery robot," in *2015 23rd Iranian Conference on Electrical Engineering*. IEEE, 2015, pp. 882–887.

10 J.-L. Bourges, J.-P. Hubschman, J. Wilson, S. Prince, T.-C. Tsao, and S. Schwartz, "Assessment of a hexapod surgical system for robotic micro-macro manipulations in ocular surgery," *Ophthalmic research*, vol. 46, no. 1, pp. 25–30, 2011.

11 "World first for robot eye operation," https://www.ox.ac.uk/news/2016-09-12-world-first-robot-eye-operation, (accessed August 6, 2020).

12 M. Motaharifar, A. Norouzzadeh, P. Abdi, A. Iranfar, F. Lotfi, B. Moshiri, A. Lashay, S. F. Mohammadi, and H. D. Taghirad, "Applications of haptic technology, virtual reality, and artificial intelligence in medical training during the COVID-19 pandemic," *Frontiers in Robotics and AI*, vol. 8, aug 2021.

13 R. Heidari, M. Motaharifar, and H. D. Taghirad, "Robust impedance control for dual user haptic training system," in *2019 7th International Conference on Robotics and Mechatronics (ICRoM)*. IEEE, nov 2019.

21 A. Hassani, "Dynamic model of arash-asist," https://github.com/aras-labs/Dynamic-Model-of-ARASH-ASiST, 2021.

14 M. Motaharifar and H. D. Taghirad, "A force reflection robust control scheme with online authority adjustment for dual user haptic system," *Mechanical Systems and Signal Processing*, vol. 135, p. 106368, 2020.

15 C.-H. Kuo and J. S. Dai, "Robotics for minimally invasive surgery: a historical review from the perspective of kinematics," in *International symposium on history of machines and mechanisms*. Springer, 2009, pp. 337–354.

16 L. Nouaille, M. A. Laribi, C. A. Nelson, S. Zeghloul, and G. Poisson, "Review of kinematics for minimally invasive surgery and tele-echography robots," *Journal of Medical Devices*, vol. 11, no. 4, 2017.

17 G. Zong, X. Pei, J. Yu, and S. Bi, "Classification and type synthesis of 1-dof remote center of motion mechanisms," *Mechanism and Machine Theory*, vol. 43, no. 12, pp. 1585–1595, 2008.

18 B. Mitchell, J. Koo, I. Iordachita, P. Kazanzides, A. Kapoor, J. Handa, G. Hager, and R. Taylor, "Development and application of a new steady-hand manipulator for retinal surgery," in *Proceedings 2007 IEEE International Conference on Robotics and Automation*. IEEE, 2007, pp. 623–629.

19 H. Meenink, "Vitreo-retinal eye surgery robot : sustainable precision," Ph.D. dissertation, Department of Mechanical Engineering, 2011.

20 L.-W. Tsai, *Robot analysis: the mechanics of serial and parallel manipulators*. John Wiley & Sons, 1999.

22 H. D. Taghirad, *Parallel robots: mechanics and control*. CRC press, 2013.

23 A. Bataleblu, R. Khorrambakht, and H. D. Taghirad, "Robust h∞-based control of ARAS-diamond: A vitrectomy eye surgery robot," *Proceedings of the Institution of Mechanical Engineers, Part C: Journal of Mechanical Engineering Science*, p. 095440622097933, dec 2020.

24 Z. Wang, Z. Liu, Q. Ma, A. Cheng, Y. hui Liu, S. Kim, A. Deguet, A. Reiter, P. Kazanzides, and R. H. Taylor, "Vision-based calibration of dual RCM-based robot arms in human-robot collaborative minimally invasive surgery," *IEEE Robotics and Automation Letters*, vol. 3, no. 2, pp. 672–679, apr 2018.

25 A. Alamdar, P. Samandi, S. Hanifeh, P. Kheradmand, A. Mirbagheri, F. Farahmand, and S. Sarkar, "Investigation of a hybrid kinematic calibration method for the "sina" surgical robot," *IEEE Robotics and Automation Letters*, vol. 5, no. 4, pp. 5276–5282, oct 2020.

26 G. A. Fontanelli, F. Ficuciello, L. Villani, and B. Siciliano, "Modelling and identification of the da vinci research kit robotic arms," in *2017 IEEE/RSJ International Conference on Intelligent Robots and Systems (IROS)*. IEEE, sep 2017.

27 A. Hassani, A. Bataleblu, S. A. Khalilpour, and H. D Taghirad, "Dynamic modeling and identification of aras-diamond: A vitreoretinal eye surgery robot," *Modares Mechanical Engineering*, vol. 21, no. 11, pp. 783–795, 2021.

28 N. S. Hojati, M. Motaharifar, H. D. Taghirad, and A. Malekzadeh, "Skill assessment using kinematic signatures: Geomagic touch haptic device," in *2019 7th International Conference on Robotics and Mechatronics (ICRoM)*. IEEE, nov 2019.